Saturation characteristics of electromagnetic ion cyclotron waves

J. Bortnik,[1] N. Omidi,[2] L. Chen,[1] R. M. Thorne,[1] and R. B. Horne[3]

[1] Electromagnetic ion cyclotron (EMIC) waves are an integral component of the Earth's dynamic space environment. In order to quantify their effect, it is necessary to know their saturation amplitude, but in modeling studies it is usually the linear growth rate that is calculated and various assumptions need to be made in order to relate this growth rate to the final amplitude of the wave. Here, we perform a comparison of the saturation characteristics of EMIC waves using a 2.5-D electromagnetic hybrid PIC code, with the corresponding linear growth rates calculated with the hot-plasma dispersion solver of the HOTRAY code. We choose a set of values consistent with satellite observations for our nominal case, and explore the parameter space in the neighborhood of this nominal case, by varying the hot proton density and thermal anisotropy. We find that the saturation amplitudes increase monotonically, and the times to saturation decrease monotonically with increasing growth rates, independent of the values of density and anisotropy. Both the saturation amplitude and time to saturation curves can be fit by simple two-parameter models with acceptable errors. This result implies that within the limitations and caveats of the present study, the saturation amplitudes and time to saturation can be predicted with good accuracy based on the linear growth rates alone, which can be used directly in conjunctions with global ring current simulations to model the resultant effects on magnetospheric particles.

Citation: Bortnik, J., N. Omidi, L. Chen, R. M. Thorne, and R. B. Horne (2011), Saturation characteristics of electromagnetic ion cyclotron waves, *J. Geophys. Res.*, *116*, A09219, doi:10.1029/2011JA016638.

1. Introduction

[2] Electromagnetic ion cyclotron (EMIC) waves are a class of naturally occurring plasma emissions that are found ubiquitously in the Earth's magnetosphere and are believed to play a key role in various dynamical processes [e.g., *Anderson et al.*, 1992a; 1992b; *Meredith et al.*, 2003; *Miyoshi et al.*, 2008; *Thorne et al.*, 2006; *Thorne*, 1974; *Ukhorskiy et al.*, 2010]. Such waves are typically excited in the L-mode near the geomagnetic equator at frequencies below the local proton gyrofrequency due to an instability associated with the thermal anisotropy of the hot proton population [*Cornwall*, 1965; *Kennel and Petschek*, 1966; *Samson*, 1991]. The EMIC waves then propagate away from the equatorial source region, roughly following geomagnetic field lines, and under certain conditions can be transmitted to the ground where they have been extensively studied as geomagnetic pulsations in the Pc1-Pc2 frequency range (0.1–5 Hz) [e.g., *Jacobs*, 1970; *Kangas et al.*, 1998].

[3] The thermal anisotropies responsible for generating EMIC waves arise naturally as plasma sheet (i.e., 1–10 keV) ions are convected Earthward from the magnetotail and subsequently carried in a westward direction around the Earth by the gradient-curvature magnetic forces along drift paths that are energy and pitch angle dependent [e.g., *Jordanova et al.*, 1994; *Kozyra et al.*, 1998]. In the inner magnetosphere, charge exchange and Coulomb scattering further enhance the anisotropy of ring current (i.e., 10–100 keV) ions [*Chen et al.*, 2010; *Daglis et al.*, 1999; *Jordanova et al.*, 1996]. In addition to convection-driven instabilities, it has been demonstrated that the compression of the dayside magnetopause can create enhanced anisotropies in off-equatorial, minimum-B pockets (Shabanski orbits) resulting in the excitation of EMIC waves [*McCollough et al.*, 2010]. Consequently, EMIC waves are most frequently observed on the dusk and day sides of the Earth, at L-shells extending from near the plasmapause all the way to the magnetopause [*Anderson et al.*, 1992b, 1992a, 1990; *Meredith et al.*, 2003], in association with increased geomagnetic activity [e.g., *Erlandson and Ukhorskiy*, 2001]. Furthermore, as hot ions drift into regions of dense, cool plasma (such as the plasmapause or plasmaspheric drainage plumes) the energies of resonant protons decrease leading to larger growth rates, and any prevailing density gradients can trap and guide the waves along the field line, thus further enhancing their path-integrated amplification [*Chen et al.*, 2009; *Thorne and Horne*, 1997].

[4] Owing to their particular spectral characteristics and typically large amplitudes (~1–10 nT) [*Erlandson and Ukhorskiy*, 2001; *Meredith et al.*, 2003], EMIC waves are implicated in a host of magnetospheric processes such as the

[1]Department of Atmospheric and Oceanic Sciences, UCLA, Los Angeles, California, USA.
[2]Solana Scientific Inc., Solana Beach, California, USA.
[3]British Antarctic Survey, Cambridge, UK.

excitation of the proton aurora [*Cornwall et al.*, 1970; *Jordanova et al.*, 2007], or the formation of stable auroral red arcs through the precipitation of thermal (few eV) electrons via Landau resonant interactions [*Cornwall et al.*, 1971; *Gurgiolo et al.*, 2005; *Thorne and Horne*, 1992]. EMIC waves are able to transfer energy to the suprathermal (~100 eV) ions [*Gary et al.*, 1995; *Roux et al.*, 1982; *Young et al.*, 1981] through cyclotron resonant interactions near the bi-ion frequency [*Horne and Thorne*, 1997], or non-resonantly through an electric phase-bunching process [e.g., *Bortnik et al.*, 2010; *Mauk et al.*, 1981; *Mauk*, 1982; *Omura et al.*, 1985]. Parasitic scattering (i.e., particle scattering that does not appreciably contribute to the wave growth or damping) of relativistic electrons and the ensuing precipitation driven by EMIC waves is believed to be a candidate for causing rapid radiation-belt electron dropout events [*Borovsky and Denton*, 2009; *Bortnik et al.*, 2006; *Desorgher et al.*, 2000; *Friedel et al.*, 2002; *Green et al.*, 2004; *Lyons and Thorne*, 1972; *Millan et al.*, 2010; *Onsager et al.*, 2007; *Shprits et al.*, 2008; *Summers and Thorne*, 2003; *Thorne and Kennel*, 1971], and the large amplitude of these waves has been demonstrated to lead to nonlinear effects, whose overall effect has yet to be fully quantified [e.g., *Albert and Bortnik*, 2009a, 2009b].

[5] In all of the processes described above, a critical parameter controlling the timescale of any dynamical changes is the amplitude of the wave. Traditionally, EMIC waves (as well as most plasma waves) are analyzed by performing instability calculations that yield a linear growth rate (either temporal or spatial) as a function of a set of input parameters. It is assumed that a plane wave with a given frequency and inclination to a static background magnetic field is propagating in a uniform plasma composed of an arbitrary number of ion species and subpopulations, each having a particular density, temperature, and anisotropy, and usually having a prescribed distribution such as a Maxwellian, but occasionally other distributions are also used [*Cattaert et al.*, 2007; *Hellberg and Mace*, 2002; *Summers et al.*, 1994; *Xue et al.*, 1993, 1996]. By scanning over a range of input parameters, the resultant growth rates reveal important characteristics such as the regions in (ω, $\mathbf{k}$) where waves are most likely to be excited (i.e., where convective growth rates maximize), or where waves will be suppressed due to enhanced damping or stop bands. The effect of various species or populations upon the wave spectral characteristics is similarly examined [*Gomberoff and Neira*, 1983; *Horne and Thorne*, 1993; *Kozyra et al.*, 1984].

[6] However, growth rates are inherently limited in that they can only provide the rate at which waves grow or damp, but cannot predict the ultimate amplitude at which the wave will stop growing (i.e., the saturation amplitude), which is the critical parameter in many applications, as outlined above. To address this shortcoming and extract a saturation amplitude based purely on growth rates, previous studies employed a semi-empirical mapping of growth rates to saturation amplitudes, based essentially on the observed range of wave amplitudes [*Jordanova*, 2003; *Jordanova et al.*, 2001, 2006, 2008]. While this approach represents an important first step, it is nevertheless unclear how accurate the actual mapping is.

[7] The aim of the present study is to produce an accurate mapping between the saturation amplitudes of EMIC waves

using a hybrid Particle In Cell (PIC) code, and linear growth rates using the HOTRAY code, for identical input parameters. In Section 2 we describe the hybrid PIC code and explore the dependence of the saturation amplitudes on a number of input parameters. In Section 3 we show the corresponding growth rates, and in Section 4 we relate the results of Sections 2 and 3. We then compare our modeled results to observed values in Section 5 and summarize our results in Section 6.

2. Hybrid Code Simulations

2.1. Code Description

[8] In order to characterize the growth and saturation of EMIC waves we employ a 2.5-D electromagnetic hybrid PIC code, in which the electromagnetic fields, currents, and ion velocities are all 3-D, while all spatial variations are confined to the 2-D X-Y plane (i.e., $\partial/\partial Z = 0$), the ions are treated as macro-particles and consist of a specified number of species and sub-populations, while the electrons are treated as a massless, charge-neutralizing fluid. This approach is targeted at studying phenomena on ion time and spatial scales, where a kinetic treatment of the electrons is not needed, as in the present case. Maxwell's equations are solved, and the displacement current in Ampere's law is neglected for computational efficiency (Darwin approximation [*Hewett*, 1994]), which results in the elimination of light waves that are not necessary for the present study. The magnetic field is advanced in time using Faraday's law and the electric field is computed from the electron momentum equation, using the electron mass $m_e = 0$ (generalized Ohm's law), and assuming quasi-neutrality so that on the resolved spatial scales the electron and ion densities are equal. This implies that electrostatic waves with very short wavelengths, i.e., of the order of or smaller than a Debye length, are excluded from the model. The electron current is related to the ion current and magnetic field by Ampere's law. The electron pressure is typically determined by an equation of state and here we assume an isothermal model. The simulation domain is assumed to be homogeneous and doubly period boundary conditions are used. This model has been used extensively in the past and is described in detail in previous publications [*Winske and Omidi*, 1996; *Winske et al.*, 2003].

2.2. Simulation of the Nominal Case

[9] We begin by simulating a case which we shall refer to as the "nominal case" and is selected to be most representative of the high L-shell, pre-noon magnetosphere. The chosen parameters are identical to those of *Bortnik et al.* [2010] and *Omidi et al.* [2010], which were in turn based on previous studies [*Anderson et al.*, 1996; *Anderson and Fuselier*, 1994; *Horne and Thorne*, 1997]. The simulation domain is contained in the X-Y plane and extends 128 proton skin depths in the X and Y directions, where each proton skin depth $\delta = c/\omega_p \approx 100$ km (here, c is the speed of light and ω_p is the ion plasma frequency). Each cell in the simulation domain measures 2×2 proton skin depths, and initially contains 64 macroparticles for each ion population or species. The plasma consists of 4 Maxwellian components, namely: (i) a charge-neutralizing fluid of massless electrons with total density $N_e = 5$ cm^{-3} and $T_\perp = T_\parallel = 0.01$ eV; (ii) a hot H$^+$
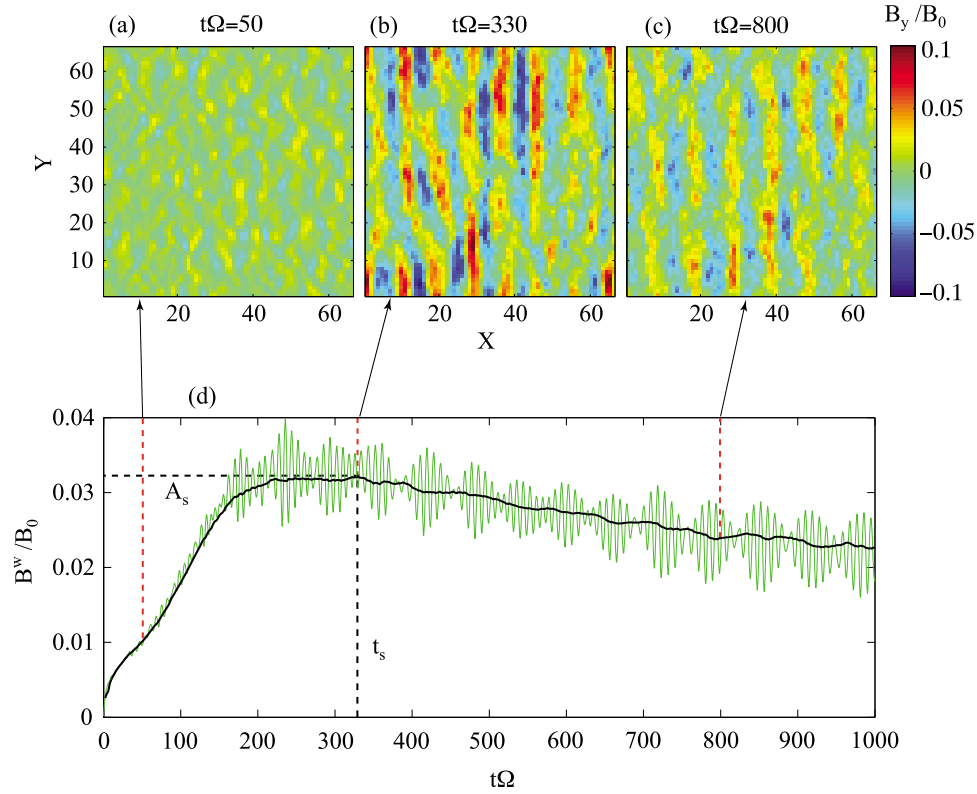
Figure 1. Snapshots of the y-component of the EMIC wave magnetic field in the X-Y plane in the (a) growth phase, $t\Omega = 50$, (b) the saturation phase, $t\Omega = 330$, and (c) the decay phase, $t\Omega = 800$. (d) The time series of B_y (green curve) and smoothed and averaged $B_y + B_z$ components (black curve) are shown.

component representing the plasma sheet with a density equal to 6% of the total density, i.e., $N_H = 0.3$ cm^{-3} with $T_\parallel = 1.3$ keV and $T_\perp = 4T_\parallel = 5.2$ keV; (iii) a cool H$^+$ component representing the majority of the background ions with a density of $N_{Hc} = 4.66$ cm^{-3} with $T_\parallel = 30$ eV and $T_\perp = 10$ eV, and (iv) a cool He$^+$ component with a density of $N_{He} = 0.04$ cm^{-3}, $T_\parallel = 20$ eV and $T_\perp = 3$ eV. The magnetic field is chosen to be $B_0 = 43$ nT in all simulations and is oriented along the X-direction.

[10] The results of the nominal case described above are displayed in Figure 1, where a component of the perpendicular magnetic field (B_y) normalized to the background field (B_0) is shown as a function of X and Y, at three different times during the simulation corresponding to the growth (Figure 1a), saturation (Figure 1b), and decay (Figure 1c) phases of the run. Figure 1d shows a profile of the wave's magnetic field intensity in the simulation domain as a function of time, which is obtained by taking the root mean square (RMS) value of each of the perpendicular magnetic components (B_y and B_z) at each time step. The profile of B_y as a function of time is shown as the green curve in Figure 1d, and the average of B_y and B_z smoothed with a 5 point moving average filter (to eliminate the rapid fluctuations) is shown using the black curve. The time axis in all cases is normalized by the proton gyrofrequency Ω, such that $t\Omega = 1000$ corresponds to ~250 s.

[11] As shown in Figure 1, the time profile of the wave magnetic field undergoes 3 basic phases, corresponding to the growth, saturation, and decay of the wave (Figures 1a–1c), which have been examined in detail by *Omidi et al.* [2010].

In the growth phase, the background noise in the simulation (roughly on the order of 10^{-4} B_0, or ~4.3 pT) is amplified by the anisotropy of the hot protons, causing a rapid increase in wave intensity, accompanied by a decrease in the hot protons' $T_\perp$, and an increase in $T_\parallel$ (i.e, a relaxation of the anisotropy). In addition, as the EMIC waves grow in intensity, they begin to transfer their power to the cool protons in a non-resonant process that has been studied in detail by *Bortnik et al.* [2010], and involves a process that has been described as electric phase bunching [e.g., *Mauk*, 1982], which has been observed in space [*Young et al.*, 1981; *Mauk et al.*, 1981; *Roux et al.*, 1982]. In this sense, the EMIC waves act as a conduit of power, funneling the free energy in the proton anisotropy to the cool ions, but themselves carrying only a small percentage of the actual energy [*Bortnik et al.*, 2010]. In the process of wave growth, the hot proton anisotropy decreases, causing the wave growth rate to decrease accordingly, and simultaneously the transfer of energy to the cool ions is enhanced due to the presence of large EMIC waves. In that sense, the system can be seen as evolving to a state of marginal stability from a region of instability [e.g., *Gary et al.*, 1994]. Wave saturation is reached when the diminished wave growth rate is exactly balanced by the rate of energy transfer to the cool ions. Further wave decay involves the continuing transfer of energy to the cool ions (where He$^+$ now dominates over H$^+$ in energy absorption).

[12] We note that although sophisticated analytical models have been developed to describe the physics of the EMIC wave growth process [*Trakhtengerts and Demekhov*, 2007; *Omura et al.*, 2010] which were based on similar ideas
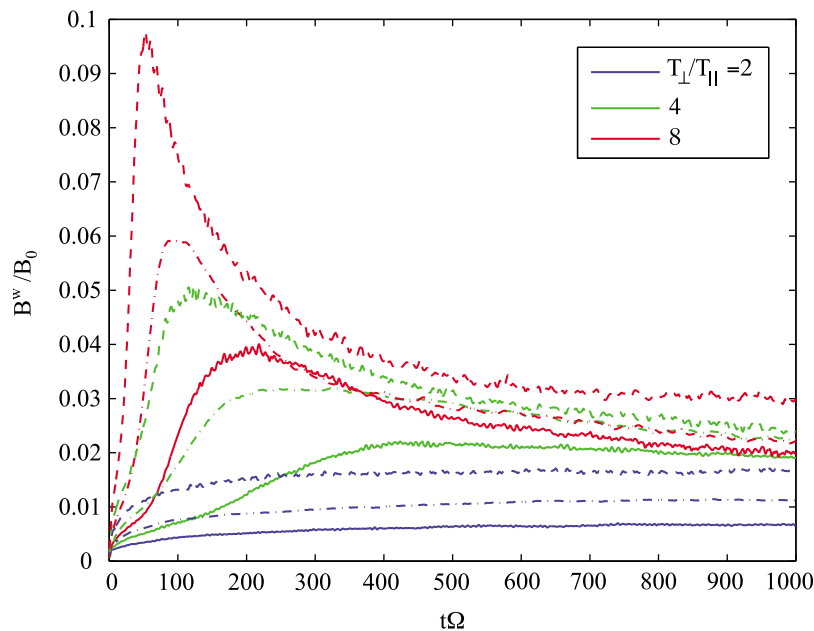
Figure 2. Averaged wave amplitude as a function of time for a combination of three levels of $T_\perp/T_\parallel = 2, 4,$ and 8 represented by the blue, green and red curves respectively), and three hot particle densities, $N_{hot} = 3\%$, 6%, and 12% represented by the solid, dash-dot and dashed lines styles respectively.

developed in the context of whistler mode wave growth [e.g., *Nunn*, 1971, 1974 *Omura and Matsumoto*, 1982; *Omura et al.*, 2008, 2009; *Trakhtengerts*, 1999] these models inherently rely on the inhomogeneity of B_0 (i.e., dB_0/dz) to generate both the wave frequency shift and the corresponding saturation value, and are thus not applicable in the present case, since our model is uniform.

[13] In comparing the time profile of the wave magnetic field to its instantaneous values shown in the snapshots, it appears that the instantaneous amplitudes reach peak values of $B_y/B_0 \sim 0.1$ (Figure 1b), whereas the Figure 1d peak is $B_w/B_0 \sim 0.032$, and is roughly a third of the peak value of Figure 1b, which merits some discussion. We believe that the way in which we estimate the total power in the system is the most meaningful for a number of reasons: first we note that in the snapshots shown in Figures 1a–1c, there are actually two sets of EMIC waves propagating in the positive and negative X-directions respectively (since the simulation domain and distribution functions are symmetrical with respect to X), and the amplitude peaks reaching $B_y/B_0 \sim 0.1$ are actually a superposition of the peak amplitudes of two counterstreaming waves, each with a peak amplitude of $B_y/B_0 \sim 0.05$, which, in the real magnetosphere would propagate away from the equatorial generation region and be observed separately in satellite surveys [e.g., *Meredith et al.*, 2003]. In addition, if we are concerned with estimating the RMS power of the wave (which is the most meaningful for estimating quasilinear diffusion rates), the peak amplitude of each EMIC wave should be reduced by a factor of $2^{1/2}$, giving a peak magnitude of roughly $B_{y, RMS}/B_0 \sim 0.05/2^{1/2} = 0.035$ which is close to our peak B_w/B_0 value. With these caveats in mind, the black curve in Figure 1d gives an adequate representation of the total amount of wave power present in the simulation domain and is also the most appropriate measure of total wave power for use in downstream models (as opposed to the peak wave intensities). For

these reasons we will be using curves derived in a similar way in the following section to study the temporal wave evolution. Using this curve we define two quantities, the saturation amplitude (A_s) of the wavefield, and the time at which saturation occurs (t_s). For the nominal case, these quantities are: $A_s = 0.032$ and $t_s = 330$ (given in units of $t\Omega$). It should be noted that since the saturation phase is fairly broad (Figure 1d), the values of t_s will contain larger variability (i.e., noise) compared to the A_s values.

2.3. Dependence on Density and Anisotropy

[14] We now aim to explore the parameter space in the neighborhood of the nominal case described in Section 2.2, and quantify the effects of varying these parameters on the saturation characteristics of the EMIC waves, specifically on the values A_s and t_s. In principle there are numerous ways to do this, including varying the parameters of the existing species, introducing additional particle species, including additional hot/cold subpopulations, and varying the shape of the distribution functions. For most of these options, interpretation of the results becomes very complex so we have chosen a simple approach, which is to vary the parameters of the hot protons only and observe the effects on the amplitude profiles. Since we have only a single species of hot ions (i.e., the H^+ ions), our approach has the advantage that we retain a fair amount of intuition regarding the expected behavior of the simulation from simple analytical approaches [*Kennel and Petschek*, 1966].

[15] We explore how the EMIC saturation scales in response to halving and doubling the total number density (N_H) and anisotropy ($T_\perp/T_\parallel$) of the hot protons, relative to the values of the nominal case. This operation yields a total of 9 combinations of parameters, the results for which are shown in Figure 2. Here, the blue, green, and red curves correspond to $T_\perp/T_\parallel = 2, 4,$ and 8 respectively, and for each of those anisotropy values, we vary the density such that the
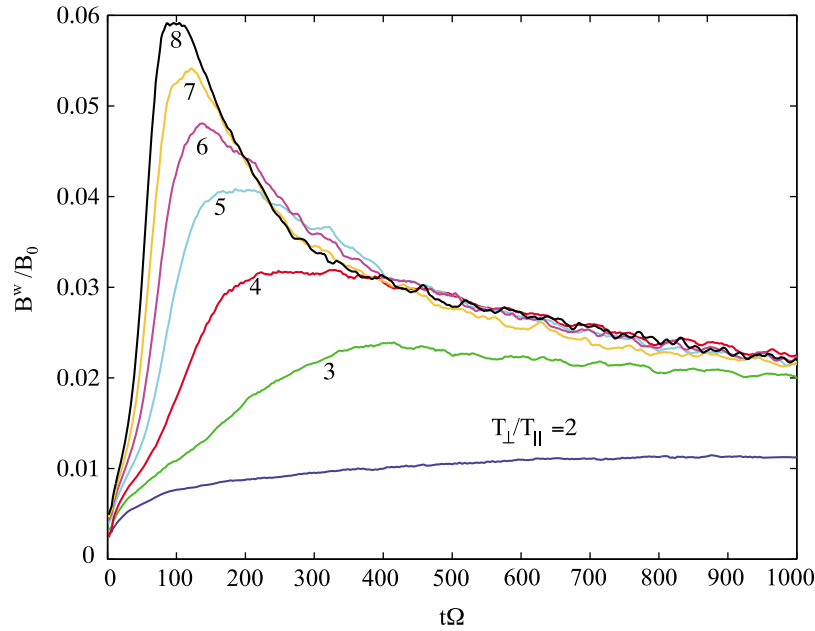
Figure 3. Curves of wave amplitude normalized to the background magnetic field B^w/B_0 shown as a function of time normalized to the proton gyroperiod, for different levels of $T_\perp/T_\parallel$ (from 2 to 8).

solid, dash-dot, and dashed curves correspond to $N_H = 3\%$, 6%, and 12% of the nominal density respectively. We note that the dash-dot green curve in Figure 2 is identical to the black curve in Figure 1d, and also that in the case where N_H is varied, the total density changes slightly and the electron density is adjusted to maintain overall charge neutrality.

[16] Figure 2 shows that A_s increases, and t_s decreases monotonically with increasing N_H as well as with increasing $T_\perp/T_\parallel$. The EMIC wave response to increasing either parameter is to reach a larger saturation amplitude, in a shorter period of time. At first glance it does not appear that the saturation curve is related in a unique way to either parameter, i.e., looking only at the wave amplitude profile we could not guess the values of N_H and $T_\perp/T_\parallel$. It also does not appear that either A_s or t_s scales linearly with density or anisotropy, in contrast to our expectation based on simple linear growth rates which depends linearly on density and anisotropy (past a critical anisotropy value).

[17] To investigate in greater detail the effect of $T_\perp/T_\parallel$ we show in Figure 3 the EMIC wave profiles for the nominal hot proton density ($N_H = 6\%$), and varying only the anisotropy over the range $T_\perp/T_\parallel = 2$–8 (shown in blue-black colors respectively) so that the top and bottom curves correspond to the dash-dot red and blue curves in Figure 2 respectively. As observed previously, increasing $T_\perp/T_\parallel$ results in a larger saturation amplitude that is achieved in a shorter period of time. Interestingly, in the decay phase of the wave amplitude, the curves appear to converge to a common value as energy is transferred non-resonantly to the thermal population [*Bortnik et al.*, 2010; *Omidi et al.*, 2010].

3. Linear Growth Rates

3.1. Calculation of the Linear Growth Rates

[18] In order for us to compare the values of A_s and t_s obtained in the previous section with their corresponding linear growth rates, it is necessary to solve the dispersion relation, i.e., find the values of n that satisfy

$$D(\mathbf{k}, \omega) = An^4 + Bn^2 + C = 0 \quad (1)$$

where the coefficients A, B, and C contain information about the EMIC wave frequency and wave normal, the background magnetic field, and a summation of the velocity space integrals over every species and subpopulation that makes up the plasma, in our case the 4 components specified in Section 2.2. For this purpose we use the HOTRAY code, which implements the full, hot dispersion relation for an arbitrary number of Maxwellian distributions, and contains the standard expansion of the dispersion relation coefficients A, B, and C given by equations (13)–(21) of *Horne* [1989]. These equations are not repeated here since they are lengthy and fairly standard, but the interested reader is referred to classic texts on the subject which give further details on their derivation [*Melrose*, 1980; *Stix*, 1992; *Swanson*, 1989].

[19] Equation (1) is solved iteratively using the Newton-Raphson method [*Press et al.*, 1992, Sections 9.4 and 9.6], by assuming a real value of k (which is taken to be field-aligned) and searching for all the complex values of $\omega = \omega_r + i\gamma$ that satisfy (1), and then repeating this procedure over all k. The convective growth rate is then obtained from the imaginary part of ω as $k_i = -\gamma/v_g$ where v_g is the group velocity.

[20] An example of a dispersion curve calculated for the parameters of the nominal case (Section 2.2) is shown in Figure 4, where the solutions of the dispersion relation for the cold plasma approximation are displayed as blue circles (as a check for the root finding method), and the solutions for the hot plasma dispersion relation are displayed as green crosses. Those $(\mathbf{k}, \omega)$ solutions with appreciable wave growth (k_i within a few orders of magnitude of its peak) are highlighted with red symbols and show that the peak growth rates occur for hydrogen band EMIC (i.e., L-mode) waves in the
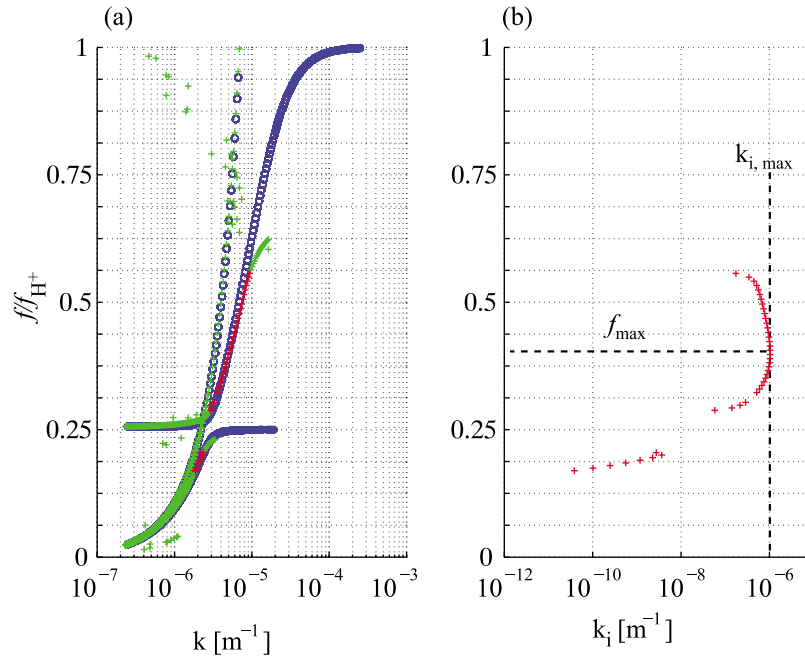
Figure 4. Solutions of the dispersion relation. (a) Real part of k, in which blue circles correspond to cold plasma solutions, green symbols correspond to the hot plasma solutions, and red symbols correspond to solutions with appreciable growth, and (b) the imaginary part.

vicinity of $\omega/\omega_H^+ \sim 0.4$, with some modest growth occurring in the helium band too. The R-mode is stable and some scatter in the solutions is evident as the wave frequency approaches the hydrogen gyroresonance frequency $\omega/\omega_H^+ = 1$.

3.2. Dependence on Density and Anisotropy

[21] We now carry out an exploration of the parameter space in the neighborhood of the nominal case values, similar to that of Section 2.2 and in preparation for a comparison of the two methods. The scaling of linear growth rates with the hot proton density N_h is trivial, since γ is proportional to N_h [*Gendrin et al.*, 1984]. We note for reference that we perform all of our linear growth calculations with $N_h = 0.1 \text{ cm}^{-3}$ which is a low enough value to ensure that the growth rate is small (i.e., $\omega_r \gg \gamma$) and the solution are stable, yet close enough to the range of densities of interest to ensure that the solutions are accurate.

[22] The scaling of k_i with anisotropy is shown in Figure 5a, where we have plotted curves similar to those of Figure 4b for values of $T_\perp/T_\parallel = 1$ to 8 (dashed curves correspond to half-integer values), and marked the peak growth rate with a red asterisk. The peak growth rates as a function of $T_\perp/T_\parallel$ are plotted in Figure 5b, and show that the peak growth rates scale roughly linearly with $T_\perp/T_\parallel$. This linear trend is consistent with our expectation based on a crude analysis of a simple 2-component plasma model (with a small component of hot protons), namely that

$$\gamma \propto \left(\frac{T_\perp}{T_\parallel} - \frac{\Omega}{\Omega - \omega} \right) \qquad (2)$$

For a peak growth rate at $\omega/\Omega = 0.4$, we expect positive growth only when $T_\perp/T_\parallel > 1.67$ or so, which is also con-

sistent with Figure 5b. We also note that according to (2), positive growth can be achieved with lower values of $T_\perp/T_\parallel$ when the EMIC wave frequency is lower, and this trend is reflected in Figure 5a which shows that the frequency of peak growth tends to decrease when $T_\perp/T_\parallel \sim 3$.

4. Comparison of Saturation Amplitudes With Linear Growth Rates

[23] We are now in a position to make a direct comparison of the linear growth rates and their corresponding saturation amplitudes calculated in the previous two sections. The values of A_s and t_s are shown in Figures 6a and 6b, where the red triangles, blue squares, and magenta circles correspond to hot proton densities of 3%, 6% and 12% respectively. For N_h values of 3% and 6% we include 3 points in each case corresponding to $T_\perp/T_\parallel = 2$, 4, and 8 (similar to Figure 2), and for $N_h = 6\%$ we include 7 points corresponding to $T_\perp/T_\parallel = 2, 3, \ldots, 8$ (similar to Figure 3). Each value of A_s and t_s is plotted against its corresponding value of the maximum growth rate k_i (shown in Figure 5), which has been properly scaled to reflect the appropriate hot proton density.

[24] The results of Figure 6 show that both A_s and t_s are organized very well by their corresponding values of maximum linear growth rates k_i. The saturation amplitude A_s shown in Figure 6a increases monotonically with increasing values of k_i independent of the specific values of density and anisotropy that have been used. After some experimentation with analytical forms, we have settled on a two-parameter fitting model:
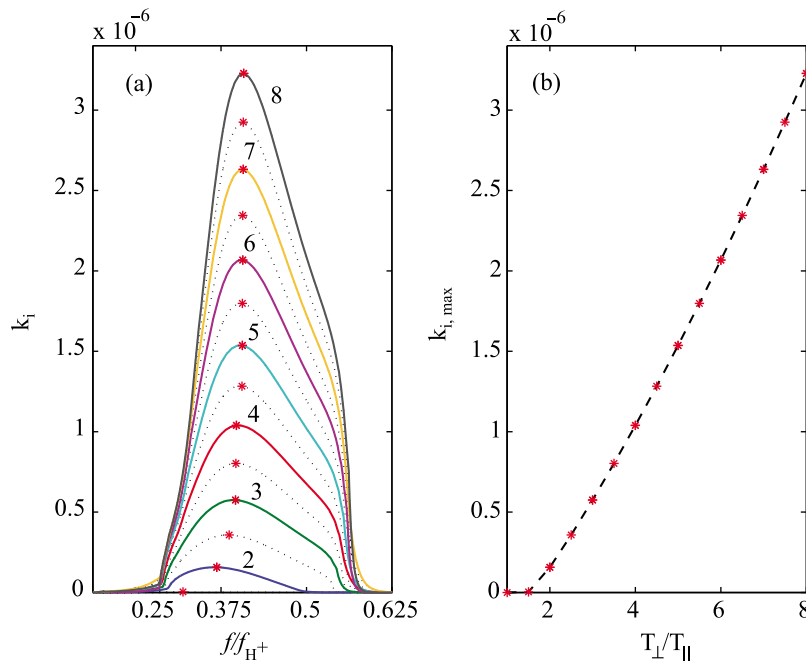
$$\hat{A}_s = a\sqrt{k_i} + bk_i \qquad (3)$$

Figure 5. Linear growth rates calculated using the HOTRAY code as a function of (a) wave frequency normalized to the Hydrogen gyrofrequency with the maximum value of k_i marked with a red asterisk, and (b) maximum value of k_i plotted as a function of thermal anisotropy.

where is the estimated value of the saturation amplitude. The parameter values that give the optimal fit are $a = 26$ m$^{1/2}$ and $b = 5000$ m, which were obtained by a global minimization of the error:

$$\varepsilon = \sqrt{\frac{1}{N}\sum_{i=1}^{N}\left(\frac{\hat{A}_s - A_s}{A_s}\right)^2} \qquad (4)$$

where N is the total number of points to be fitted (13 in our case). The optimal values of (a, b) give an error of $\sum$ = 4.7%, which is considered very good when compared to the errors associated with the input parameters obtained from real observational results [*Kremser et al.*, 1985].

[25] The time to saturation values t_s shown in Figure 6b monotonically decrease as a function of increasing k_i and can be fit with the two-parameter model:

$$\hat{t}_s = \frac{c}{k_i + d} \qquad (5)$$

analogously with (3) above. The optimal-fit values are c = 3.6 × 10^{-4} and d = 3 × 10−7 m^{-1} which result in an error of $\sum$ = 19%. This error is significantly higher than the corresponding value associated with the saturation amplitude, which was expected due to the larger amount of noise associated with the identification of the t_s value (see discussion in section 2.2).

5. Comparison of Saturation Amplitudes With Observed Values

[26] We can check the reasonableness of our model by performing a comparison of the observed EMIC wave characteristics in the same region where we obtained our plasma characteristics. Focusing on the outer magnetoshere (L ~9) in the dawn and day sides [*Anderson et al.*, 1992b] reports the observation of predominantly left-hand circularly polarized EMIC waves, with average normalized frequencies in the range of ω/Ω ~0.4–0.5, and average intensities in the range of 1.6 nT to 2.5 nT corresponding to the dawn and day sides respectively. Comparing with our Figures 4 and 5, the linear growth rates maximize for left-hand circularly polarized waves with peak growth rates falling in the range of normalized frequencies of ω/ω_H^+ ~0.37–0.44, consistent with the observations. Using our typical simulated saturation amplitudes shown in Figures 2, 3, and 6a of 0.01–0.06 together with our assumed background field gives average wave intensities of 0.4–2.6 nT, again in good agreement with typical observed EMIC wave amplitudes in that region.

[27] Although we have used parameters for our nominal case that are typical of the dawn-day outer magnetosphere, the results of this study can be applied more generally to other regions of the magnetosphere. For example, using typical storm-time parameters calculated for the November 2–6, 1993 magnetic storm [*Kozyra et al.*, 1997] with the Ring current Atmosphere interaction Model (RAM) code [*Jordanova et al.*, 1996, 1994], *Thorne and Horne* [1997] modeled the peak growth rates of EMIC waves in the inner magnetosphere near L = 4.25 (where B_0 ~390 nT) with $N_{hot} = 14$ cm^{-3}, $N_{cold} = 140$ cm^{-3} (such that N_{hot}/N_{cold} = 10%) and of $T_\perp/T_\parallel$ ~1.56. Reading the dashed blue curve in Figure 2 which corresponds to N_h = 12%, $T_\perp/T_\parallel$ = 2 (i.e., roughly similar values), gives a saturation amplitude of A_s ~1% of the background field value or ~4 nT, again, in reasonable agreement with observed values [*Anderson et al.*, 1992b; *Erlandson and Ukhorskiy*, 2001]. We note that a
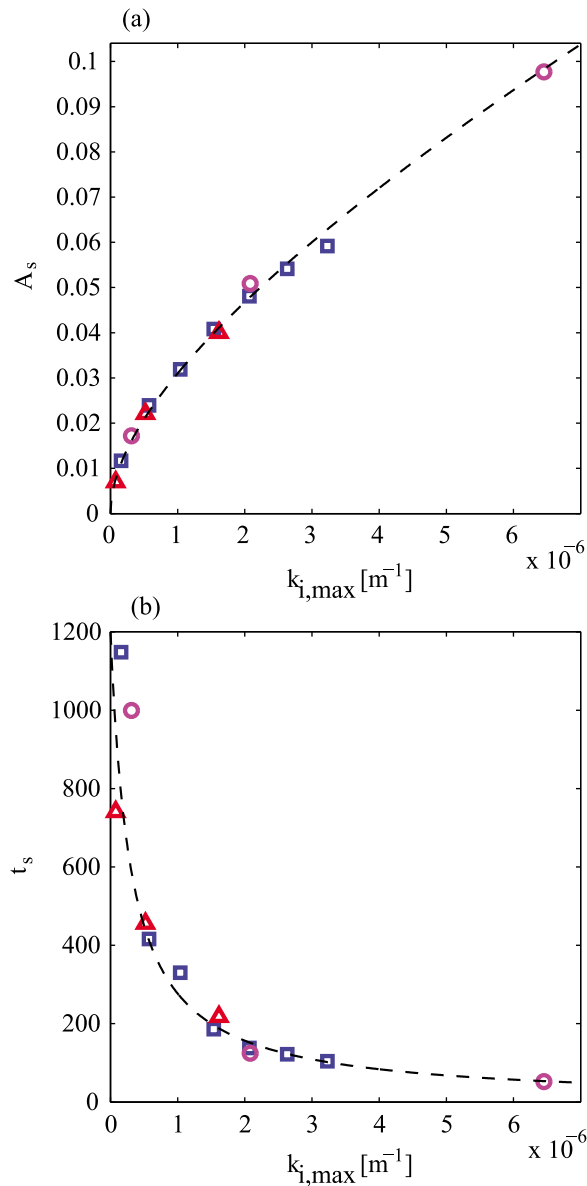
Figure 6. (a) Saturation amplitude A_s and (b) time to saturation t_s plotted as a function of maximum growth rate $k_{i,max}$. The red triangles, blue squares, and magenta circles represent hot plasma densities of 3%, 6% and 12% respectively. The dashed curve in each panel is the optimal least squares fit.

more direct comparison cannot be made since [*Thorne and Horne*, 1997] have a component of hot Oxygen ions which is not included in our present model.

6. Summary and Conclusions

[28] We performed a model-model comparison to determine whether a simple relationship existed between the linear growth rates of EMIC waves, and their corresponding saturation characteristics (namely the saturation amplitude A_s and time to saturation t_s). The saturation amplitude is a key quantity which is necessary in calculating diffusion coefficients for a variety of applications. The standard approach in previous work has been to calculate linear growth rates

using the distribution functions of several species and subpopulations, but this approach is limited in that it cannot predict what the saturation amplitude of the wave will be, and so a semi-empirical mapping between growth rates and their corresponding saturation amplitudes was made, whose validity is uncertain. On the other hand, simulations using particle-in-cell (PIC) codes give detailed spatiotemporal profiles of the growth and saturation of the waves, but they are computationally intensive, and impractical to perform over a large array of input parameters in the context of global simulations.

[29] To address this problem, we compared the saturation characteristics of a 2.5-D electromagnetic hybrid PIC code, with the corresponding linear growth rates calculated with the hot-plasma dispersion solver of the HOTRAY code. We chose a set of values consistent with satellite observations for our nominal case, and explored the parameter space in the neighborhood of the nominal case, by varying the hot proton density and thermal anisotropy. We found that the saturation amplitudes increased monotonically, and the time to saturation decreased monotonically with increasing growth rates, independent of the values of density and anisotropy. Both the saturation amplitudes and time to saturation curves could be fit by simple two-parameter models with acceptable errors. This result implies that within the limitations and caveats of the present study (e.g., uniform background field, single hot species, and fixed concentration of cool ions), the saturation amplitudes (and time to saturation if necessary) can be predicted with good accuracy based on the linear growth rates alone, which can be used directly in global ring current simulations.

References

Albert, J. M., and J. Bortnik (2009a), Correction to "Nonlinear interaction of radiation belt electrons with electromagnetic ion cyclotron waves," *Geophys. Res. Lett.*, *36*, L24101, doi:10.1029/2009GL041850.

Albert, J. M., and J. Bortnik (2009b), Nonlinear interaction of radiation belt electrons with electromagnetic ion cyclotron waves, *Geophys. Res. Lett.*, *36*, L12110, doi:10.1029/2009GL038904.

Anderson, B. J., and S. A. Fuselier (1994), Response of thermal ions to electromagnetic ion cyclotron waves, *J. Geophys. Res.*, *99*(A10), 19,413–19,425, doi:10.1029/94JA01235.

Anderson, B. J., K. Takahashi, R. E. Erlandson, and L. J. Zanetti (1990), Pc1 pulsations observed by AMFTE/CCE in the Earth's outer magnetosphere, *Geophys. Res. Lett.*, *17*(11), 1853–1856, doi:10.1029/GL017i011p01853.

Anderson, B. J., R. E. Erlandson, and L. J. Zanetti (1992a), A statistical study of Pc 1–2 magnetic pulsations in the equatorial magnetosphere: 1. Equatorial occurrence distributions, *J. Geophys. Res.*, *97*(A3), 3075–3088, doi:10.1029/91JA02706.

Anderson, B. J., R. E. Erlandson, and L. J. Zanetti (1992b), A statistical study of Pc 1–2 magnetic pulsations in the equatorial magnetosphere: 2. Wave properties, *J. Geophys. Res.*, *97*(A3), 3089–3101, doi:10.1029/91JA02697.

Anderson, B. J., R. E. Denton, G. Ho, D. C. Hamilton, S. A. Fuselier, and R. J. Strangeway (1996), Observational test of local proton cyclotron instability in the Earth's magnetosphere, *J. Geophys. Res.*, *101*(A10), 21,527–21,543, doi:10.1029/96JA01251.

Borovsky, J. E., and M. H. Denton (2009), Relativistic-electron dropouts and recovery: A superposed epoch study of the magnetosphere and the solar wind, *J. Geophys. Res.*, *114*, A02201, doi:10.1029/2008JA013128.

Bortnik, J., R. M. Thorne, T. P. O'Brien, J. C. Green, R. J. Strangeway, Y. Y. Shprits, and D. N. Baker (2006), Observation of two distinct,

rapid loss mechanisms during the 20 November 2003 radiation belt drop-out event, *J. Geophys. Res.*, *111*, A12216, doi:10.1029/2006JA011802.

Bortnik, J., R. M. Thorne, and N. Omidi (2010), Nonlinear evolution of EMIC waves in a uniform magnetic field: 2. Test-particle scattering, *J. Geophys. Res.*, *115*, A12242, doi:10.1029/2010JA015603.

Cattaert, T., M. A. Hellberg, and R. L. Mace (2007), Oblique propagation of electromagnetic waves in a kappa-Maxwellian plasma, *Phys. Plasmas*, *14*, 082111, doi:10.1063/1.2766647.

Chen, L., R. M. Thorne, and R. B. Horne (2009), Simulation of EMIC wave excitation in a model magnetosphere including structured high-density plumes, *J. Geophys. Res.*, *114*, A07221, doi:10.1029/2009JA014204.

Chen, L., R. M. Thorne, V. K. Jordanova, C.-P. Wang, M. Gkioulidou, L. R. Lyons, and R. B. Horne (2010), Global simulation of EMIC wave excitation during the 21 April 2001 storm from coupled RCM-RAM-HOTRAY modeling, *J. Geophys. Res.*, *115*, A07209, doi:10.1029/2009JA015075.

Cornwall, J. M. (1965), Cyclotron instabilities and electromagnetic emission in the ultra low frequency and very low frequency ranges, *J. Geophys. Res.*, *70*(1), 61–69, doi:10.1029/JZ070i001p00061.

Cornwall, J. M., F. Coroniti, and R. M. Thorne (1970), Turbulent loss of ring current protons, *J. Geophys. Res.*, *75*(25), 4699–4709, doi:10.1029/JA075i025p04699.

Cornwall, J. M., F. V. Coroniti, and R. M. Thorne (1971), Unified theory of SAR arc formation at the plasmapause, *J. Geophys. Res.*, *76*(19), 4428–4445, doi:10.1029/JA076i019p04428.

Daglis, I. A., R. M. Thorne, W. Baumjohann, and S. Orsini (1999), The terrestrial ring current: Origin, formation, and decay, *Rev. Geophys.*, *37*(4), 407–438, doi:10.1029/1999RG900009.

Desorgher, L., P. Buhler, A. Zehnder, and E. O. Fluckiger (2000), Simulation of the outer radiation belt electron flux decrease during the March 26, 1995, magnetic storm, *J. Geophys. Res.*, *105*(A9), 21,211–21,223, doi:10.1029/2000JA900060.

Erlandson, R. E., and A. Y. Ukhorskiy (2001), Observations of electromagnetic ion cyclotron waves during geomagnetic storms: Wave occurrence and pitch angle scattering, *J. Geophys. Res.*, *106*(A3), 3883–3895, doi:10.1029/2000JA000083.

Friedel, R. H. W., G. D. Reeves, and T. Obara (2002), Relativistic electron dynamics in the inner magnetosphere—A review, *J. Atmos. Sol. Terr. Phys.*, *64*, 265–282, doi:10.1016/S1364-6826(01)00088-8.

Gary, S. P., M. B. Moldwin, M. F. Thomsen, D. Winske, and D. J. McComas (1994), Hot proton anisotropies and cool proton temperatures in the outer magnetosphere, *J. Geophys. Res.*, *99*(A12), 23,603–23,615.

Gary, S. P., M. F. Thomsen, Y. Lin, and D. Winske (1995), Electromagnetic proton cyclotron instability: Interaction with magnetospheric protons, *J. Geophys. Res.*, *100*, 21,961–21,972, doi:10.1029/95JA01403.

Gendrin, R., M. Ashour-Abdalla, Y. Omura, and K. Quest (1984), Linear analysis of ion cyclotron interaction in a multicomponent plasma, *J. Geophys. Res.*, *89*(A10), 9119–9124, doi:10.1029/JA089iA10p09119.

Gomberoff, L., and R. Neira (1983), Convective growth rate of ion cyclotron waves in a H+-He+ and H+-He+-O+ plasma, *J. Geophys. Res.*, *88*(A3), 2170–2174, doi:10.1029/JA088iA03p02170.

Green, J. C., T. G. Onsager, T. P. O'Brien, and D. N. Baker (2004), Testing loss mechanisms capable of rapidly depleting relativistic electron flux in the Earth's outer radiation belt, *J. Geophys. Res.*, *109*, A12211, doi:10.1029/2004JA010579.

Gurgiolo, C., B. R. Sandel, J. D. Perez, D. G. Mitchell, C. J. Pollock, and B. A. Larsen (2005), Overlap of the plasmasphere and ring current: Relation to subauroral ionospheric heating, *J. Geophys. Res.*, *110*, A12217, doi:10.1029/2004JA010986.

Hellberg, M. A., and R. L. Mace (2002), Generalized plasma dispersion function for a plasma with a kappa-Maxwellian velocity distribution, *Phys. Plasmas*, *9*(5), 1495, doi:10.1063/1.1462636.

Hewett, D. W. (1994), Low-frequency electromagnetic (Darwin) applications in plasma simulation, *Comput. Phys. Commun.*, *84*, 243–277, doi:10.1016/0010-4655(94)90214-3.

Horne, R. B. (1989), Path-integrated growth of electrostatic waves: The generation of terrestrial myriametric radiation, *J. Geophys. Res.*, *94*(A7), 8895–8909.

Horne, R. B., and R. M. Thorne (1993), On the preferred source location for the convective amplification of ion cyclotron waves, *J. Geophys. Res.*, *98*(A6), 9233–9247, doi:10.1029/92JA02972.

Horne, R. B., and R. M. Thorne (1997), Wave heating of He+ by electromagnetic ion cyclotron waves in the magnetosphere: Heating near the H+-He+ bi-ion resonance frequency, *J. Geophys. Res.*, *102*(A6), 11,457–11,471, doi:10.1029/97JA00749.

Jacobs, J. A. (1970), *Geomagnetic Micropulsations*, Springer, New York.

Jordanova, V. K. (2003), Ring current asymmetry from global simulations using a high-resolution electric field model, *J. Geophys. Res.*, *108*(A12), 1443, doi:10.1029/2003JA009993.

Jordanova, V. K., J. U. Kozyra, G. V. Khazanov, A. F. Nagy, C. E. Rasmussen, and M. C. Fok (1994), A bounce-averaged kinetic model of the ring current ion population, *Geophys. Res. Lett.*, *21*(25), 2785–2788, doi:10.1029/94GL02695.

Jordanova, V. K., L. M. Kistler, J. U. Kozyra, G. V. Khazanov, and A. F. Nagy (1996), Collisional losses of ring current ions, *J. Geophys. Res.*, *101*(A1), 111–126, doi:10.1029/95JA02000.

Jordanova, V. K., C. J. Farrugia, R. M. Thorne, G. V. Khazanov, G. D. Reeves, and M. F. Thomsen (2001), Modeling ring current proton precipitation by electromagnetic ion cyclotron waves during the May 14–16, 1997, storm, *J. Geophys. Res.*, *106*, 7–22, doi:10.1029/2000JA002008.

Jordanova, V. K., Y. S. Miyoshi, S. Zaharia, M. F. Thomsen, G. D. Reeves, D. S. Evans, C. G. Mouikis, and J. F. Fennell (2006), Kinetic simulations of ring current evolution during the Geospace Environment Modeling challenge events, *J. Geophys. Res.*, *111*, A11S10, doi:10.1029/2005JA011644.

Jordanova, V. K., M. Spasojevic, and M. F. Thomsen (2007), Modeling the electromagnetic ion cyclotron wave-induced formation of detached sub-auroral proton arcs, *J. Geophys. Res.*, *112*, A08209, doi:10.1029/2006JA012215.

Jordanova, V. K., J. Albert, and Y. Miyoshi (2008), Relativistic electron precipitation by EMIC waves from self-consistent global simulations, *J. Geophys. Res.*, *113*, A00A10, doi:10.1029/2008JA013239.

Kangas, J., A. Guglielmi, and O. Pokhotelov (1998), Morphology and physics of short-period magnetic pulsations, *Space Sci. Rev.*, *83*(3–4), 435–512, doi:10.1023/A:1005063911643.

Kennel, C. F., and H. E. Petschek (1966), Limit on stably trapped particles, *J. Geophys. Res.*, *71*(1), 1–28.

Kozyra, J. U., T. E. Cravens, A. F. Nagy, E. G. Fontheim, and R. S. B. Ong (1984), Effects of energetic heavy ions on electromagnetic ion cyclotron wave generation in the plasmapause region, *J. Geophys. Res.*, *89*(A4), 2217–2233, doi:10.1029/JA089iA04p02217.

Kozyra, J. U., V. K. Jordanova, R. B. Horne, and R. M. Thorne (1997), Modelling of the contribution of electromagnetic ion cyclotron (EMIC) waves to stormtime ring current erosion, in *Magnetic Storms*, *Geophys. Monogr. Ser.*, edited by B. T. Tsurutani et al., pp. 187–202, AGU, Washington, D. C.

Kozyra, J. U., V. K. Jordanova, J. E. Borovsky, M. F. Thomsen, D. J. Knipp, D. S. Evans, D. J. McComas, and T. E. Cayton (1998), Effects of a high-density plasma sheet on ring current development during the November 2–6, 1993, magnetic storms, *J. Geophys. Res.*, *103*(A11), 26,285–26,305, doi:10.1029/98JA01964.

Kremser, G., W. Studemann, B. Wilken, G. Gloeckler, D. C. Hamilton, F. M. Ipavich, and D. Hovestadt (1985), Charge state distributions of Oxygen and Carbon in the energy range 1 to 300 keV/e observed with AMPTE/CCE in the magnetosphere, *Geophys. Res. Lett.*, *12*(12), 847–850, doi:10.1029/GL012i012p00847.

Lyons, L. R., and R. M. Thorne (1972), Parasitic pitch angle diffusion of radiation belt particles by ion cyclotron waves, *J. Geophys. Res.*, *77*(28), 5608–5616, doi:10.1029/JA077i028p05608.

Mauk, B. H. (1982), Electromagnetic wave energization of heavy ions by the electric "phase bunching" process, *Geophys. Res. Lett.*, *9*(10), 1163, doi:10.1029/GL009i010p01163.

Mauk, B. H., C. E. McIlwain, and R. L. McPherron (1981), Helium cyclotron resonance within the Earth's magnetosphere, *Geophys. Res. Lett.*, *8*, 103–106, doi:10.1029/GL008i001p00103.

McCollough, J. P., S. R. Elkington, M. E. Usanova, I. R. Mann, D. N. Baker, and Z. C. Kale (2010), Physical mechanisms of compressional EMIC wave growth, *J. Geophys. Res.*, *115*, A10214, doi:10.1029/2010JA015393.

Melrose, D. B. (1980), *Plasma Astrophysics: Nonthermal Processes in Diffuse Magnetized Plasmas*, vol. 1, *The Emission, Absorption and Transfer of Waves in Plasmas*, Gordon and Breach, New York.

Meredith, N. P., R. M. Thorne, R. B. Horne, D. Summers, B. J. Fraser, and R. R. Anderson (2003), Statistical analysis of relativistic electron energies for cyclotron resonance with EMIC waves observed on CRRES, *J. Geophys. Res.*, *108*(A6), 1250, doi:10.1029/2002JA009700.

Millan, R. M., K. B. Yando, J. C. Green, and A. Y. Ukhorskiy (2010), Spatial distribution of relativistic electron precipitation during a radiation belt depletion event, *Geophys. Res. Lett.*, *37*, L20103, doi:10.1029/2010GL044919.

Miyoshi, Y., K. Sakaguchi, K. Shiokawa, D. S. Evans, J. M. Albert, M. Connoers, and V. K. Jordanova (2008), Precipitation of radiation belt electrons by EMIC waves, observed from ground and space, *Geophys. Res. Lett.*, *35*, L23101, doi:10.1029/2008GL035727.

Nunn, D. (1971), A theory of VLF emissions, *Planet. Space Sci.*, *19*, 1141–1167, doi:10.1016/0032-0633(71)90110-3.

Nunn, D. (1974), A self-consistent theory of triggered VLF emissions, *Planet. Space Sci.*, *22*, 349–378, doi:10.1016/0032-0633(74)90070-1.

Omidi, N., R. M. Thorne, and J. Bortnik (2010), Nonlinear evolution of EMIC waves in a uniform magnetic field: 1. Hybrid simulations, *J. Geophys. Res.*, *115*, A12241, doi:10.1029/2010JA015607.

Omura, Y., and H. Matsumoto (1982), Computer simulations of basic processes of coherent whistler wave-particle interactions in the magnetosphere, *J. Geophys. Res.*, *87*, 4435–4444, doi:10.1029/JA087iA06p04435.

Omura, Y., M. Ashour-Abdalla, R. Gendrin, and K. Quest (1985), Heating of thermal helium in the equatorial magnetosphere: A simulation study, *J. Geophys. Res.*, *90*, 8281–8292, doi:10.1029/JA090iA09p08281.

Omura, Y., Y. Katoh, and D. Summers (2008), Theory and simulation of the generation of whistler-mode chorus, *J. Geophys. Res.*, *113*, A04223, doi:10.1029/2007JA012622.

Omura, Y., M. Hikishima, Y. Katoh, D. Summers, and S. Yagitani (2009), Nonlinear mechanisms of lower-band and upper-band VLF chorus emissions in the magnetosphere, *J. Geophys. Res.*, *114*, A07217, doi:10.1029/2009JA014206.

Omura, Y., J. Pickett, B. Grison, O. Santolik, I. Dandouras, M. Engebretson, P. M. E. Décréau, and A. Masson (2010), Theory and observation of electromagnetic ion cyclotron triggered emissions in the magnetosphere, *J. Geophys. Res.*, *115*, A07234, doi:10.1029/2010JA015300.

Onsager, T. G., J. C. Green, G. D. Reeves, and H. J. Singer (2007), Solar wind and magnetospheric conditions leading to the abrupt loss of outer radiation belt electrons, *J. Geophys. Res.*, *112*, A01202, doi:10.1029/2006JA011708.

Press, W. H., S. A. Teukolsky, W. T. Vetterling, and B. P. Flannery (1992), *Numerical Recipes in C: The art of Scientific Computing*, 2nd ed., Cambridge Univ. Press, Cambridge, U. K.

Roux, A., S. Perraut, J. L. Rauch, C. D. Villedary, G. Kremser, A. Korth, and D. T. Young (1982), Wave-particle interactions near Ω_{He+} observed on board GEOS 1 and 2: 2. Generation of ion cyclotron waves and heating of He$^+$ ions, *J. Geophys. Res.*, *87*(A10), 8174–8190, doi:10.1029/JA087iA10p08174.

Samson, J. C. (1991), Geomagnetic pulsations and plasma waves in the Earth's magnetosphere, in *Geomagnetism*, vol. 4, pp. 481–592, Acad. Press, London.

Shprits, Y., D. Subbotin, N. Meredith, and S. Elkington (2008), Review of modeling of losses and sources of relativistic electrons in the outer radiation belt II: Local acceleration and loss, *J. Atmos. Sol. Terr. Phys.*, *70*(14), 1694–1713, doi:10.1016/j.jastp.2008.06.014.

Stix, T. H. (1992), *Waves in Plasmas*, 2nd ed., Springer, New York.

Summers, D., and R. M. Thorne (2003), Relativistic electron pitch-angle scattering by electromagnetic ion cyclotron waves during geomagnetic storms, *J. Geophys. Res.*, *108*(A4), 1143, doi:10.1029/2002JA009489.

Summers, D., S. Xue, and R. M. Thorne (1994), Calculation of the dielectric tensor for a generalized Lorentzian (kappa) distribution function, *Phys. Plasmas*, *1*(6), 2012–2025, doi:10.1063/1.870656.

Swanson, D. G. (1989), *Plasma Waves*, Academic, Boston, Mass.

Thorne, R. M. (1974), The consequences of micropulsations on geomagnetically trapped particles, *Space Sci. Rev.*, *16*(3), 443–458, doi:10.1007/BF00171568.

Thorne, R. M., and R. B. Horne (1992), The contribution of ion-cyclotron waves to electron heating and SAR-arc excitation near the storm-time plasmapause, *Geophys. Res. Lett.*, *19*(4), 417–420, doi:10.1029/92GL00089.

Thorne, R. M., and R. B. Horne (1997), Modulation of electromagnetic ion cyclotron instability due to interaction with ring current O+ during magnetic storms, *J. Geophys. Res.*, *102*(A7), 14,155–14,163, doi:10.1029/96JA04019.

Thorne, R. M., and C. F. Kennel (1971), Relativistic electron precipitation during magnetic storm main phase, *J. Geophys. Res.*, *76*(19), 4446–4453, doi:10.1029/JA076i019p04446.

Thorne, R. M., R. B. Horne, V. K. Jordanova, J. Bortnik, and S. A. Glauert (2006), Interaction of EMIC waves with thermal plasma and radiation belt particles, in *Magnetospheric ULF Waves: Synthesis and New Directions*, Geophys. Monogr. Ser., vol. 169, edited by K. Takahashi et al., pp. 213–223, AGU, Washington D. C.

Trakhtengerts, V. Y. (1999), A generation mechanism for chorus emissions, *Ann. Geophys.*, *17*, 95–100.

Trakhtengerts, V. Y., and A. G. Demekhov (2007), Generation of Pc 1 pulsations in the regime of backward wave oscillator, *J. Atmos. Sol. Terr. Phys.*, *69*, 1651–1656, doi:10.1016/j.jastp.2007.02.009.

Ukhorskiy, A. Y., Y. Y. Shprits, B. J. Anderson, K. Takahashi, and R. M. Thorne (2010), Rapid scattering of radiation belt electrons by storm-time EMIC waves, *Geophys. Res. Lett.*, *37*, L09101, doi:10.1029/2010GL042906.

Winske, D., and N. Omidi (1996), A nonspecialist's guide to kinetic simulations of space plasmas, *J. Geophys. Res.*, *101*(A8), 17,287–17,303, doi:10.1029/96JA00982.

Winske, D., L. Yin, N. Omidi, H. Karimabadi, and K. Quest (2003), Hybrid simulation codes: Past, present and future–A tutorial, in *Space Plasma Simulation*, edited by J. Buchner, C. T. Dum, and M. Scholer, pp. 136–165, Springer, Berlin, doi:10.1007/3-540-36530-3_8.

Xue, S., R. M. Thorne, and D. Summers (1993), Electromagnetic ion-cyclotron instability in space plasmas, *J. Geophys. Res.*, *98*(A10), 17,475–17,484, doi:10.1029/93JA00790.

Xue, S., R. M. Thorne, and D. Summers (1996), Growth and damping of oblique electromagnetic ion cyclotron waves in the Earth's magnetosphere, *J. Geophys. Res.*, *101*(A7), 15,457–15,466, doi:10.1029/96JA01088.

Young, D. T., S. Perraut, A. Roux, C. D. Villedary, R. Gendrin, A. Korth, G. Kremser, and D. Jones (1981), Wave-particle interactions near Ω_{He+} observed on GEOS 1 and 2: 1. Propagation of ion cyclotron waves in He$^+$-rich plasma, *J. Geophys. Res.*, *86*(A8), 6755–6772, doi:10.1029/JA086iA08p06755.

J. Bortnik, L. Chen, and R. M. Thorne, Department of Atmospheric and Oceanic Sciences, UCLA, Math Sciences Building, Rm. 7115, Los Angeles, CA 90095, USA. (jbortnik@atmos.ucla.edu)

R. B. Horne, British Antarctic Survey, Cambridge CB3 0ET, UK.

N. Omidi, Solana Scientific Inc., Solana Beach, CA 92075, USA.